



RESEARCH ARTICLE

10.1029/2018JA025639

Key Points:

- Measured profiles of the energetic electron energy flux and characteristic energies in Jupiter's main auroral region
- Data help constrain Jovian auroral acceleration theories - various aspects in agreement with both Knight and MHD turbulence predictions
- Comparisons to Hisaki remote sensing data reveal that the hydrocarbon eddy diffusion coefficient in the auroral region may be enhanced

Correspondence to:

G. Clark,
george.clark@jhuapl.edu

Citation:

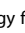
























Clark, G., Tao, C., Mauk, B. H., Nichols, J., Saur, J., Bunce, E. J., et al. (2018). Precipitating electron energy flux and characteristic energies in Jupiter's main auroral region as measured by Juno/JEDI. *Journal of Geophysical Research: Space Physics*, 123. <https://doi.org/10.1029/2018JA025639>

Received 6 MAY 2018

Accepted 4 AUG 2018

Accepted article online 17 AUG 2018

Precipitating Electron Energy Flux and Characteristic Energies in Jupiter's Main Auroral Region as Measured by Juno/JEDI

G. Clark¹ , C. Tao² , B. H. Mauk¹ , J. Nichols³ , J. Saur⁴ , E. J. Bunce³ , F. Allegrini^{5,6} , R. Gladstone⁵ , F. Bagenal⁷ , S. Bolton⁵ , B. Bonfond⁸ , J. Connerney^{9,10} , R. W. Ebert⁵ , D. J. Gershman⁹ , D. Haggerty¹ , T. Kimura¹¹ , P. Kollmann¹ , S. Kotsiaros⁹ , W. S. Kurth¹² , S. Levin¹³ , D. J. McComas^{5,14} , G. Murakami¹⁵ , C. Paranicas¹ , A. Rymer¹ , and P. Valek^{5,6} 

¹The Johns Hopkins University Applied Physics Laboratory, Laurel, MD, USA, ²National Institute of Information and Communications Technology, Tokyo, Japan, ³Department of Physics and Astronomy, University of Leicester, Leicester, UK, ⁴Institut für Geophysik und Meteorologie, Universität zu Köln, Cologne, Germany, ⁵Southwest Research Institute, San Antonio, TX, USA, ⁶Department of Physics and Astronomy, University of Texas at San Antonio, San Antonio, TX, USA, ⁷Laboratory for Atmospheric and Space Physics, University of Colorado Boulder, Boulder, CO, USA, ⁸Space Sciences, Technologies and Astrophysics Research Institute, LPAP, Université de Liège, Liège, Belgium, ⁹Goddard Space Flight Center, Greenbelt, MD, USA, ¹⁰Space Research Corporation, Annapolis, MD, USA, ¹¹Frontier Research Institute for Interdisciplinary Sciences, Tohoku University, Sendai, Japan, ¹²Department of Physics and Astronomy, University of Iowa, Iowa City, IA, USA, ¹³Jet Propulsion Laboratory, Pasadena, CA, USA, ¹⁴Department of Astrophysical Sciences, Princeton University, Princeton, NJ, USA, ¹⁵Institute of Space and Astronautical Science, Japan Aerospace Exploration Agency, Sagami-hara, Japan

Abstract The relationship between electron energy flux and the characteristic energy of electron distributions in the main auroral loss cone bridges the gap between predictions made by theory and measurements just recently available from Juno. For decades such relationships have been inferred from remote sensing observations of the Jovian aurora, primarily from the Hubble Space Telescope, and also more recently from Hisaki. However, to infer these quantities, remote sensing techniques had to assume properties of the Jovian atmospheric structure—leading to uncertainties in their profile. Juno's arrival and subsequent auroral passes have allowed us to obtain these relationships unambiguously for the first time, when the spacecraft passes through the auroral acceleration region. Using Juno/Jupiter Energetic particle Detector Instrument (JEDI), an energetic particle instrument, we present these relationships for the 30-keV to 1-MeV electron population. Observations presented here show that the electron energy flux in the loss cone is a nonlinear function of the characteristic or mean electron energy and supports both the predictions from Knight (1973, [https://doi.org/10.1016/0032-0633\(73\)90093-7](https://doi.org/10.1016/0032-0633(73)90093-7)) and magnetohydrodynamic turbulence acceleration theories (e.g., Saur et al., 2003, <https://doi.org/10.1029/2002GL015761>). Finally, we compare the in situ analyses of Juno with remote Hisaki observations and use them to help constrain Jupiter's atmospheric profile. We find a possible solution that provides the best agreement between these data sets is an atmospheric profile that more efficiently transports the hydrocarbons to higher altitudes. If this is correct, it supports the previously published idea (e.g., Parkinson et al., 2006, <https://doi.org/10.1029/2005JE002539>) that precipitating electrons increase the hydrocarbon eddy diffusion coefficients in the auroral regions.

1. Introduction

Our understanding of Jupiter's auroral acceleration processes is rapidly evolving since the arrival of NASA's Juno mission to Jupiter. Juno observations have revealed the presence of diverse electron and ion populations associated with both the upward and downward auroral current regions in Jupiter's polar magnetosphere. Recently published results focusing on the particle observations have shown the presence of both broadband and peaked electron energy distributions in both the downward (Allegrini et al., 2017; Mauk et al., 2017a, 2017b, 2018) and upward (Clark, Mauk, Haggerty, et al., 2017; Ebert et al., 2017) loss cones. The auroral ion observations revealed the presence of energetic ion conics (Clark, Mauk, Haggerty, et al., 2017), parallel potential drops (Clark, Mauk, Haggerty, et al., 2017; Haggerty et al., 2017; Mauk et al., 2017b, 2018), and stochastic processes likely associated with wave-particle interactions (Elliott et al., 2018; Li et al., 2017; Louarn et al., 2017; Ma et al., 2017; Mauk et al., 2018). Perhaps one of the more surprising discoveries is the role that broadband

©2018. Johns Hopkins Applied Physics Laboratory.

This is an open access article under the terms of the Creative Commons Attribution License, which permits use, distribution and reproduction in any medium, provided the original work is properly cited.

acceleration plays in the generation of Jupiter's powerful aurora. Mauk et al. (2017b, 2018) showed that broadband or stochastic electron distributions are associated with the most intense auroras at Jupiter, which are fundamentally different from Earth's aurora. How these distributions are accelerated in the auroral region and their link between the magnetosphere and ionosphere are still mysteries. Here we provide clues that further our understanding of these processes by comparing Juno's in situ energetic particle observations with various acceleration theories as well as remote sensing observations from Juno and Hisaki.

In this paper we focus primarily on the main auroral region, that is, the region that couples the main auroral emissions in the ionosphere to the region of corotation breakdown in the middle magnetosphere (e.g., Hill, 1979, 2001; Hill et al., 1981; Cowley & Bunce, 2001). Embedded in this region is a magnetic field-aligned current system that is generated by angular momentum transfer between the ionosphere and magnetosphere (e.g., Cowley et al., 2003; Grodent, 2015; Hill, 2001, and references therein). Cowley and Bunce (2001) were the first to recognize that the unaccelerated, hot magnetospheric electron population measured by Voyager (Scudder et al., 1981) does not have enough energy flux or current density in the loss cone to explain the bright auroral emissions observed by the Hubble Space Telescope (HST; e.g., Gérard et al., 2014; Gustin et al., 2004). This led them to adopt the Knight relationship (Knight, 1973) from Earth to Jupiter. They found that parallel potentials on the order of ~ 100 kilovolts (kV) must develop to accelerate the current carriers to provide current densities that commensurate with Jupiter's bright aurora. Following Cowley and Bunce (2001), several studies (e.g., Cowley, 2006; Nichols & Cowley, 2004, 2005; Ray et al., 2009, 2010) used the Knight relation at Jupiter; however, each study imposed slightly different physical conditions. Details regarding these studies are discussed in section 3.

In contrast to the Knight relation, Saur et al. (2002, 2003) took a different approach and hypothesized that the coupling between the weak magnetohydrodynamic (MHD) turbulence and Jupiter's global current system produces a field-aligned accelerating electric potential. In this theory, the energy in the turbulence cascade is dissipated via Joule heating (Saur et al., 2003, their equation (2)). Using values for the energy flux and current density measured by the Galileo spacecraft (Khurana, 2001; Kivelson et al., 2004), Saur et al. (2003) calculated a parallel potential around 160 kV, which agrees well with Cowley and Bunce's (2001) estimate. Saur et al. (2003) provided a current-voltage relationship that is based on an effective Alfvén conductance and assumes the dissipation occurs at the electron inertial length scale at high latitudes through wave-particle interactions.

The acceleration theories above were compared to the inferred electron characteristic energies derived from HST remote sensing observations (e.g., Gérard et al., 2003; 2014; Gustin et al., 2004). These studies have used the multispectral observations of the far ultraviolet spectrum from Hubble's Space Telescope Imaging Spectrograph to derive the ratio of the H_2 emission intensities at wavelengths between 155–162 and 123–130 nm. This is referred to as the color ratio (e.g., Gérard et al., 2014). The shorter wavelength emissions are partly absorbed by the hydrocarbons, whereas the longer wavelengths are not attenuated. Determining the altitude of the partly absorbed emissions allows one to use this ratio and determine the characteristic energy of the precipitating electrons; however, it is sensitive to the assumed altitude profile of the hydrocarbon column density (e.g., Gérard et al., 2003; Tao et al., 2016), and thus, the inferred characteristic energies can vary by factors of 2–5. In 2013, JAXA launched Hisaki (Yoshikawa et al., 2014), an Earth-orbiting satellite, which makes spectral observations (80–148 nm) of the emissions from Jupiter's auroral region and the Io plasma torus. Unlike HST, Hisaki does not have the spatial resolution to resolve the highly structured Jovian aurora. However, it does have the ability to perform long-term monitoring, which is extremely useful. Using a similar method employed by HST, the color ratio maps derived by Hisaki (Tao et al., 2016) show similar characteristic electron energies, that is, approximately tens to hundreds of keV. Although HST and Hisaki data have provided much of our understanding of the phenomenological nature of Jupiter's aurora, the variation in the derived parameters and the sensitivity to the unconstrained CH_4 profile left large uncertainties when trying to distinguish between auroral acceleration theories and Magnetosphere-Ionosphere (MI) coupling processes.

We provide here, for the first time, the in situ precipitating electron energy flux versus characteristic energy profiles in Jupiter's main auroral region. In addition, we compare these profiles with those hypothesized by the acceleration mechanisms described above, as well as with the remote sensing observations with Hisaki. Section 2 describes in detail the energetic particle observations made by the Jupiter Energetic particle Detector Instrument (JEDI). In section 3, we provide further details on the theoretical acceleration

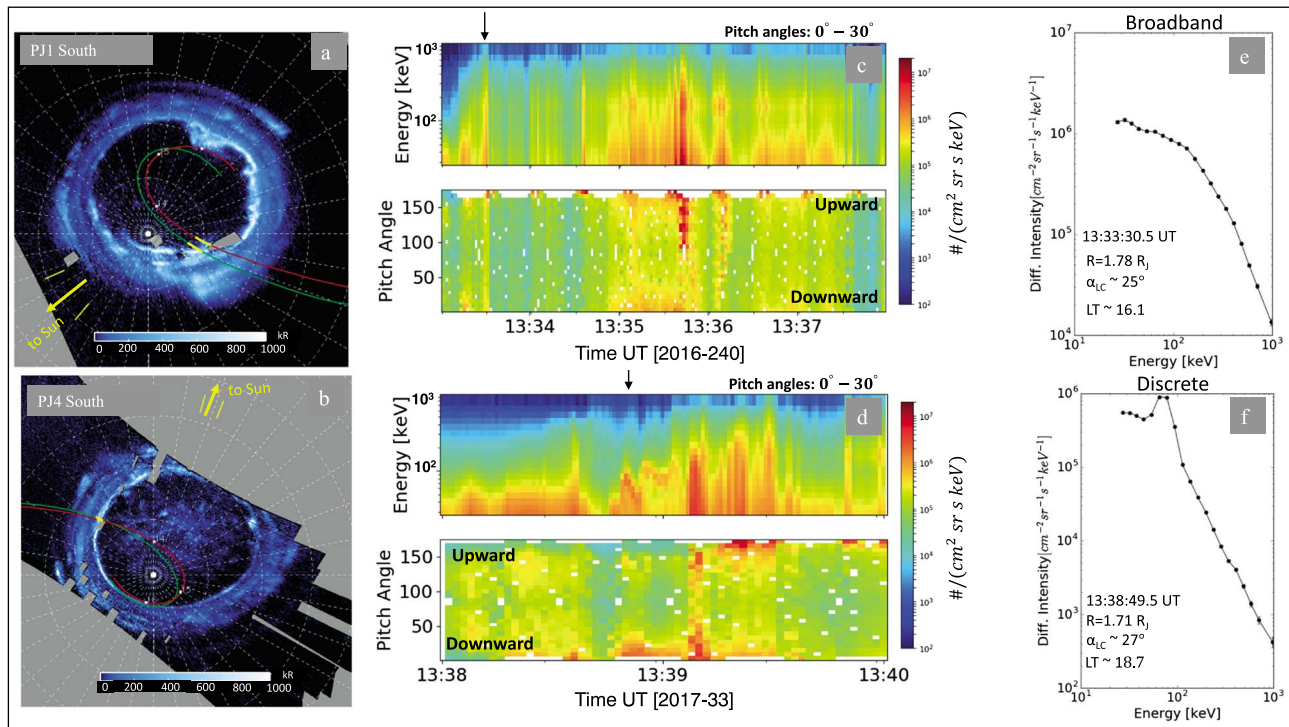


Figure 1. Juno/UVS and Juno/JEDI observations of the main aurora to illustrate the two general types of electron distribution associated with this region, similar to that shown in Mauk et al. (2017b). Top panel: UV emissions of the southern auroral oval during PJ1 with the Juno trajectory superimposed based off the VIP4+CAN (red) and VIPAL (green) magnetic field models. Yellow bars near the main oval indicate times corresponding to the Juno/JEDI observations. Yellow arrow and bars near the edge of plot show direction to Sun and its location at the start and end time of the UVS data time interval (panel a); energy and pitch angle versus time of the >30 -keV electrons during a snapshot of the main auroral crossing. White blanks in the spectrogram are used to represent *fill* values or no data (panel c); energy spectrum corresponding to the time illustrated by the black arrow in panel (e). The spectrum illustrates the broadband energy profile that lacks any distinct peaks and has been associated with stochastic acceleration. Bottom panel: Same format as top panel, but now for the southern auroral excursion during PJ4 (panels b, d and f). The example in this panel depicts the peaked energy distribution typically associated with discrete or inverted-V-type acceleration. JEDI = Jupiter Energetic particle Detector Instrument; PJ = perijove; UVS = ultraviolet spectrometer; LT = local time.

mechanisms and discuss their comparisons with experimental measurements. In section 4 we compare Juno and Hisaki observations and discuss our findings and interpretations in section 5.

2. Energetic Electron Observations

We present energetic electron observations from Juno/JEDI, an instrument that comprises three sensors mounted $\sim 120^\circ$ apart on the spacecraft deck. Two of these sensors are mounted such that their field of view (FOV) is optimized to measure field-aligned charged particles. These are the JEDI 90 and JEDI 270 sensors. See Mauk et al., 2017 for a detailed description of the JEDI instrument. For this study, it is important to note that JEDI can measure the energy and angular distributions of ~ 30 keV to 1 MeV electrons. A single sensor is made up of six solid state detector (SSD) telescopes, each with an instantaneous full width at half maximum FOV of $\sim 9^\circ \times 17^\circ$ (Mauk et al., 2018; see their supporting information). The accumulation time during the high rate is ~ 0.5 s, but we find averaging over 1 second is necessary to avoid poor statistics. This corresponds to approximately 12° in spacecraft rotation. The calculations we perform below can be biased if JEDI is not properly resolving the loss cone; therefore, we only consider times/locations when Juno traversed the main auroral field lines at altitudes below ~ 2.5 Jovian radii (R_J). All the low-altitude crossings of the auroral field lines occurred over a range from 1.3 to $1.79 R_J$. This is because the geometric loss cone at these altitudes is larger than $\sim 15^\circ$, and thus, JEDI's angular FOV is adequate to resolve the loss cone distributions. Pitch angle determination is based on the local magnetic field measurements from Juno/MAG (Connerney et al., 2017).

Figure 1 shows the two types of precipitating auroral electron distributions typically observed with JEDI associated with magnetic field crossings connected to the main aurora, presumably under the acceleration

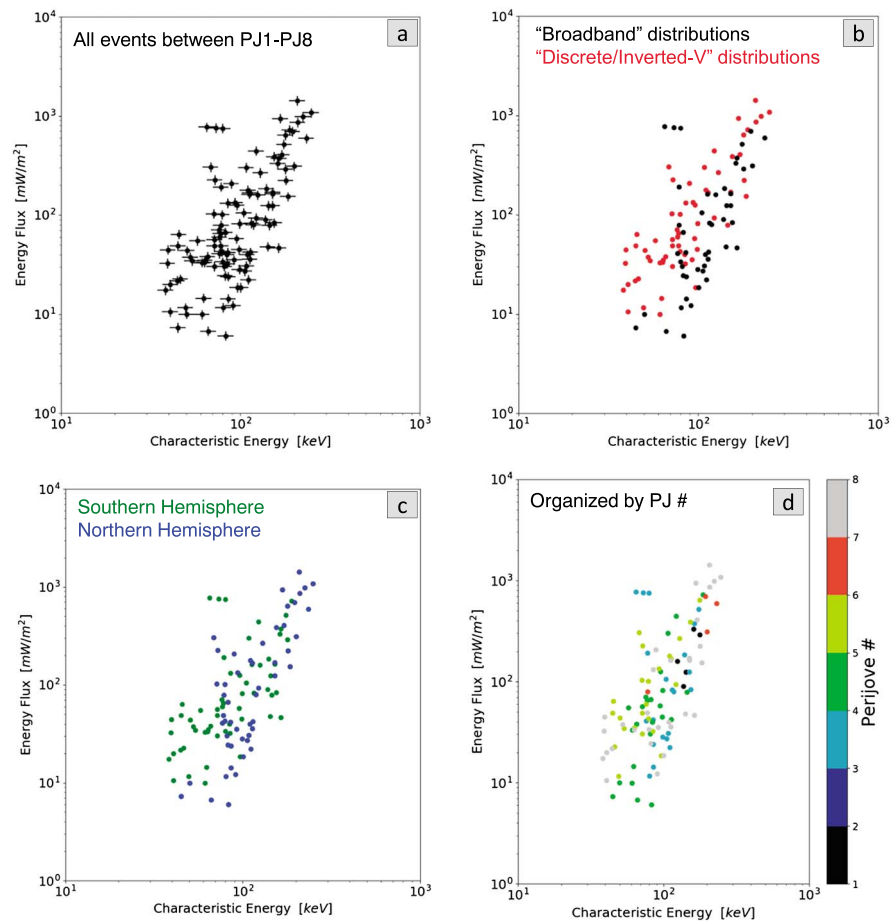


Figure 2. Relationships of >30 -keV electron energy flux as a function of characteristic energy obtained by Juno/Jupiter Energetic particle Detector Instrument spanning PJs 1–8. Each panel is configured the same, but the data are represented slightly differently. Panel (a) includes error bars; panels (b)–(d) distinguish the types of electron distributions, the hemisphere in which they were observed and the PJ number, respectively. PJ = perijove.

region. The images in Figures 1a and 1b are produced by the Juno ultraviolet spectrometer instrument. The color represents the photon intensity and the thick red line is Juno’s projected magnetic footprint onto the ionosphere. To perform the projection, we used the VIP4+CAN and VIPAL magnetic field models (Connerney et al., 1981, 1998; Hess et al., 2011). Figures 1c and 1d are the corresponding electron energy and pitch angle distributions measured by JEDI during the times indicated on the auroral images. The black arrow in Figure 1c illustrates the time period chosen to display the energy spectrum (Figure 1e), which can be characterized as a broadband energy distribution with no sharp peaks possibly indicating no coherent acceleration structure. Similarly, in Figure 1d the black arrow illustrates the time of the electron spectrum in Figure 1f. This energy distribution clearly shows a sharp peak, that is, nonmonotonic spectrum, at ~ 100 keV indicating a coherent acceleration process (Figure 1f), possibly a localized magnetic field-aligned potential drop above the spacecraft. In the first case (Figure 1c), the electrons are bidirectional with both the upward and downward loss cones populated. In the second case (Figure 1d), the electrons are primarily field-aligned and downward moving. These two examples have been discussed in detail by Mauk et al. (2017b). We chose these specific examples because they illustrate two possibly different acceleration mechanisms. It should be noted that at other times Juno has also observed true power law distributions in the main auroral region as well as slightly different variants of the broadband spectrum with no peak. Such distributions will be shown in Figure 3 that is discussed later in the sections.

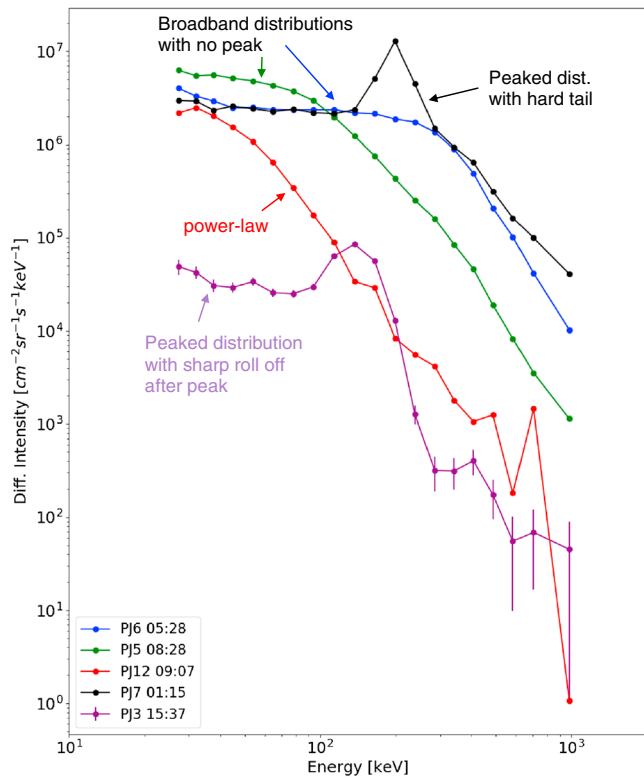


Figure 3. Examples of the various types of energy spectra found in Jupiter’s low-altitude main auroral region. The blue and green curves illustrate the broadband energy distributions, with no peak, that have different roll-off energies. The purple and black curves illustrate peaked energy distributions with a soft tail and a hard tail, respectively, occurring after the peak. Lastly, the red curve shows a power law distribution. PJ = perijove.

An important point of this study is the directly measured relationship between the energy flux and characteristic energy of the precipitating electrons; therefore, we discuss how we derive these quantities. First, the characteristic energy is defined as the mean energy of the electron distribution as shown in equation (1). In the absence of sharply defined peaks, we calculate the characteristic energy as the ratio of energy flux to the number flux (Mauk et al., 2004), $\langle E \rangle = I_E/I_n$, where I_E is the energy flux or the third moment of the distribution function and I_n is the number flux or first moment. The moments are defined in Mauk et al. (2004).

$$E = \frac{I_E}{I_N} = \frac{\int_{E_{\min}}^{E_{\max}} I \cdot E \, dE}{\int_{E_{\min}}^{E_{\max}} I \, dE} \quad (1)$$

where I is the charged particle differential intensity in units of $\text{keV}^{-1} \cdot \text{cm}^{-2} \cdot \text{s}^{-1} \cdot \text{sr}^{-1}$. In the presence of a peaked energy distribution, that is, parallel potential drop, we can either use the previous method or infer the mean energy by calculating the centroid of the peak. Either method provides a numerical result that is within the uncertainty of JEDI’s energy response. To calculate the energy flux projected to the ionosphere, we use the factor of π which represents the area-projected-weighted loss cone (Mauk et al., 2017a)

$$\epsilon_l = \pi \int_{E_{\min}}^{E_{\max}} I \cdot E \, dE \quad (2)$$

where E_{\min} and E_{\max} are the geometric means corresponding to the limits of JEDI’s energy response, which are ~ 27 and 979 keV respectively. Errors associated with these parameters are calculated by propagating JEDI’s $\sim 20\%$ energy resolution and Poisson counting statistics.

Figure 2 shows the profiles of the measured electron energy flux as a function of the characteristic energy for times when Juno crossed the low-altitude magnetic field lines connecting to the main aurora (Northern and Southern Hemispheres). Collectively, the points represent measurements spanning perijove (PJ) 1 to PJ8. Note that JEDI’s lower energy range for electrons is ~ 30 keV. The largest characteristic or peaked energies observed in the main auroral region are ~ 300 – 400 keV, in agreement with those observed in previous case study event (Mauk et al., 2017b). The majority of the points cluster together and depict a nonlinear trend—a factor of 10 increase in characteristic energy produces roughly ~ 100 increase in energy flux. In Figure 2b we distinguish the points associated with the broadband energy (no peak) distributions and those with peaked (nonmonotonic) distributions. Figures 2c and 2d color code the measurements by the Northern and Southern Hemispheres and the PJ number, respectively. An interesting pattern that emerges is the similar energy flux relationship between both the broadband with no peak distributions and those that show a clear peak. For characteristic energies greater than ~ 100 keV the populations are clearly intermixed; however, there may be a difference below ~ 80 keV, but there is significant scatter in the energy flux. Why or how do two seemingly distinct acceleration processes produce similar relationships? This is an unexpected result and we discuss it further in section 4.

As mentioned previously, there are several types of energetic electron distributions associated with the main aurora. Previous publications have focused on two general types: broadband with no peak and the peaked distributions (Allegrini et al., 2017; Clark, Mauk, Paranicas, et al., 2017; Ebert et al., 2017; Mauk et al., 2017a, 2017b, 2018). Here we expand the list and show the various types of electron distributions (Figure 3) associated with the main auroral crossings. Figure 3 illustrates five types of energy spectra (intensity as a function of electron energy) with four qualitative differences. (1) The peaked energy distribution with a soft tail that drops off dramatically after the peak (Figure 3, purple curve). These sorts of distributions are thought to be associated with parallel potential structures in the auroral acceleration region (Clark, Mauk, Haggerty, et al., 2017; Mauk et al., 2017b). They almost always exhibit a plateau in differential intensity below the peak energy,

which is also evident in the broadband energy distributions. (2) The peaked energy distribution that has a hard tail that extends upward to megaelectron volt energies after the peak (Figure 3, black curve). This particular event was discussed by Mauk et al. (2017b), and it occurred during a time when the electron distributions evolved from the characteristic inverted-V-type profile (black on Figure 3) to a more broadband distribution with no peak. This was concluded to be evidence of an instability initiating while Juno was passing through the acceleration region. (3) The power law distribution (red curve), occurs less often than the other types. Whether it is a marker of another type of auroral acceleration process or the manifestation of the peaked or broadband with no peak is still unclear. It is certainly possible that energy diffusion due to wave-particle processes can redistribute the broadband spectra. (4) Another common type of spectrum is the broadband spectrum with no peak (blue and green curves). These distributions typically exhibit a flattop or plateau from lower energies until a rollover energy where the spectrum falls off with increasing energy, that is, power law like. The rollover energy can occur anywhere between tens and hundreds of kiloelectron volts. In section 4 we further discuss the physical interpretation of these different types of auroral electron populations.

JEDI observations are not without their own limitations. Here we discuss potential shortcomings owing to instrumental responses and assumptions made in calculating the energy flux and characteristic energy profiles.

Electric potential between the spacecraft and ionosphere. Unless the data suggested otherwise, we assumed that no significant electric potential existed below the spacecraft, that is, between the spacecraft and Jupiter's auroral region. If there was a significant potential then the loss cone and energy weighting done by the calculations to obtain energy flux and characteristic energy would be wrong. Out of all the events analyzed, only the auroral crossing on 2017–192 at ~02:34:40 UT showed evidence for a significant potential structure between the spacecraft and Jupiter. In this case, the precipitating electrons in the loss cone exhibit a broadband energy spectrum; however, the upward moving electrons show evidence of peaked energy distributions as high as ~200–300 keV, which may suggest parallel potential drops below the spacecraft. For this particular event we altered the loss cone size based on the electric potential (Clark, Mauk, Haggerty, et al., 2017). The ion distributions in some of the other events displayed complex behavior, which makes it difficult to infer a direct current (DC) potential drop below the spacecraft and therefore no higher-order corrections were implemented. For example, the upward ions in the PJ7 01:15:45 UT event analyzed by Mauk et al. (2018) exhibit both intermittent broadband and peaked distributions. It is unclear if this is due to wave-particle interactions, a potential drop below the spacecraft, or a combination of the two. Within the same event, there are also times when the energetic ions disappear. It can also be argued that because we observe the inverted-V potential structures then by definition the particles are falling through the full electric potential above the spacecraft and there is no reason to believe a significant portion resides below the spacecraft.

Pitch angle coverage. JEDI's angular coverage and resolution is not perfect. Close inspection of the pitch angle distributions (PADs) in Figure 1 reveals that on occasion, JEDI is *blind* to small pitch angle sectors within the loss cone (represented by the white pixels/blanks). As mentioned above, we restricted the events to the low-altitude auroral crossings to mitigate this effect, but we must recognize that albeit however small, the energy flux calculations represent a lower limit. In general, JEDI's pitch angle coverage of the field-aligned particles will only get worse as Juno's orbit evolves. This is because two of the three sensors have their FOV primarily in a plane perpendicular to the spin axis and as Juno's apojove precesses toward Jupiter's nightside the FOV is no longer nearly instantaneously sampling all pitch angles. Instead, it will measure the full PAD approximately every 30 s.

Exclusion of plasma observations (energies <30 keV). Historically, space plasmas are typically segregated into at least two populations: energies less than ~20–40 keV and greater than 30 keV. This division is primarily driven by different instrumental techniques required to measure the full distribution function. A more rigorous approach would utilize the multiple instruments on Juno, and at the time of writing, intercalibration efforts are ongoing between JEDI and Jovian Auroral Distribution Experiment (JADE; McComas et al., 2017), and here we chose to primarily focus on the energetic electrons. Therefore, the energy fluxes presented in this study should be interpreted as a lower limit. Nonetheless, energy fluxes were spot checked during one auroral pass to be sure no gross mistakes were being made. Importantly, JADE and JEDI were reporting similar energy fluxes (within a factor of 3 or so) for overlapping energies between 30 and 100 keV. (JADE is unique in that it is a plasma sensor that can measure electrons up to 100 keV.)

In the following two sections (3 and 4) we compare the measured relationships discussed in this section to those predicted by two types of theories: the Knight relation (Knight, 1973) and dissipation of turbulent electromagnetic field fluctuations (Saur et al., 2003). In addition, we also compare the in situ characteristics with those inferred previously by remote sensing observations and discuss the similarities and differences.

3. Data/Theory Comparison

3.1. Knight Relation

If the magnetospheric population is an isotropic Maxwellian velocity distribution then in the absence of a field-aligned voltage, that is, the field line is an equipotential, the energy flux of the electrons in the loss cone is given by (e.g., Cowley & Bunce, 2001, and references therein)

$$E_F(0) = 2NW_{th} \left(\frac{W_{th}}{2\pi m_e} \right)^{1/2} \quad (3)$$

where N and W_{th} are the density and thermal energy respectively of the current carrying population. As Cowley and Bunce (2001) point out, the typical values used for the hot magnetospheric electron population outside the equatorial plasma sheet come from Voyager measurements (Scudder et al., 1981) and are $N \cong 0.01 \text{ cm}^{-3}$ and $W_{th} \cong 2.5 \text{ keV}$. The m_e is the mass of the electron. As discussed in section 1, this energy flux is hundreds of times less than what is needed to drive Jupiter's powerful aurora. Knight's relation (Knight, 1973) considers the properties of field-aligned potentials required to drive field-aligned currents, under the assumption that the accelerator is compact and located high above the ionosphere. Cowley and Bunce (2001, their equation (38)) give the energy flux relationship as

$$EF(\Phi, R_B) = \frac{1}{2} E_F(0) R_B \left[\left(2 + \frac{e\Phi}{W_{th}} \right) - \left(\frac{e\Phi}{W_{th}} + 2 \left(1 - \frac{1}{R_B} \right) \right) \exp \left(\frac{-e\Phi}{W_{th}(R_B - 1)} \right) \right] \quad (4)$$

where $e\Phi$ is the energy gained by the electrons falling through the potential drop. R_B is the ratio of the magnetic field strength in the ionosphere and the field strength at the top of the voltage drop. For example, a ratio of 27, that is, $R_B = (B_i/B_\phi) = 27$, puts the voltage drop, or acceleration region, at $\sim 3 R_J$. However, although not always explicit in the literature, the calculated accelerating voltage is often the minimum accelerating voltage computed under the simplifying assumption that $R_B \rightarrow \infty$, which effectively places the top of the voltage drop at infinity. When this is the case, equation (4) reduces to (Cowley & Bunce, 2001; see their equation (39) and Figure 7)

$$EF(\Phi, R_B \rightarrow \infty) = E_F(0) \left[1 + \left(\frac{e\Phi}{W_{th}} \right) + \frac{1}{2} \left(\frac{e\Phi}{W_{th}} \right)^2 \right] \quad (5)$$

The above energy flux relationships were calculated in the nonrelativistic regime; however, because the characteristic energies associated with Jupiter's aurora are often as high as a few hundred kiloelectron volts, we also compare the data with Cowley's (2006, see their equation (34)) expression for relativistic electrons in the limit that $R_B \rightarrow \infty$.

$$EF_{rel}(\Phi, R_B \rightarrow \infty) = E_F(0) \left[1 + \left(\frac{e\Phi}{W_{th}} \right) + \frac{1}{2} \left(\frac{e\Phi}{W_{th}} \right)^2 + \frac{1}{2} \frac{\left(\frac{e\Phi}{W_{th}} \right)^3}{\left(2 \left(\frac{m_e c^2}{W_{th}} \right) + 3 \right)} \right] \quad (6)$$

3.2. Turbulence Theory

The hypothesis that large potential drops develop at Jupiter as a consequence of the coupling between the weak MHD turbulence in the equatorial region and the global current system was first put forth by Saur et al. (2003). Assuming, for simplicity, that the electric currents are dominated by small scale fluctuations and all the wave energy goes into stochastic electron acceleration, the energy flux relationship is as follows

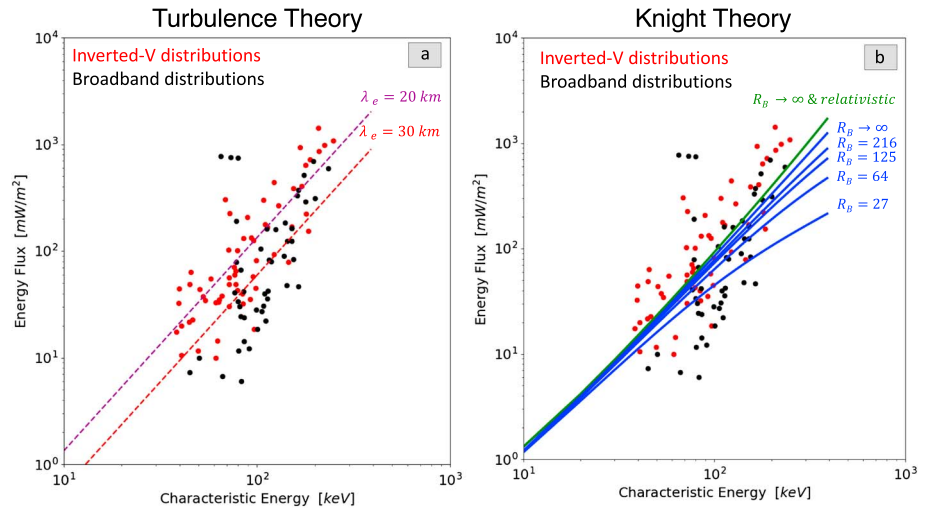


Figure 4. Comparison between Juno/Jupiter Energetic particle Detector Instrument measurements and auroral acceleration theories. (a) MHD turbulence theory utilizes equation (7) for two different electron inertial length scales, 20 km (purple dashed curve) and 30 km (red dashed curve). The various forms of Knight’s relationships come from equations (4)–(6). The green curve illustrates the relativistic case in the limit that $R_B \rightarrow \infty$. The other various blue curves are for the nonrelativistic cases, but with varying R_B . The corresponding altitudes in Jovian radii for the acceleration region locations are $R_B = 216, 125, 64$ and $27 \rightarrow 6R_J, 5R_J, 4R_J, 3R_J$ respectively (Cowley & Bunce, 2001).

$$EF_{\text{turbulence}}(\Phi) = \frac{\Sigma_A}{\lambda_e^2} \Phi^2 \quad (7)$$

Σ_A is an effective Alfvén conductance, that is, $\Sigma_A = (\mu_o v_A)^{-1}$ where μ_o is the permeability of free space and v_A is the Alfvén velocity, which scales with the magnetic field and plasma mass density. We assume here that it is half the speed of light, that is, $v_A = 0.5c$. The λ_e is the electron inertial length scale ($\lambda_e = c/\omega_{pe}$, where c is the speed of light and ω_{pe} is the plasma frequency), which is estimated to be ~ 20 to 30 km (which corresponds to bulk electron densities of 0.07 and 0.03 cm^{-3} , respectively). The electron densities used here are reasonable and are the same order of magnitude of the Scudder et al. (1981) values.

3.3. The Relationship Between Electron Characteristic Energies and Field-Aligned Electric Potentials

The theories presented above provide relationships between the electron energy flux and total parallel potential drop along the magnetic field line (s). Juno lacks a D.C. electric field instrument, so we rely on the electron distributions to guide our interpretation of the electric potentials in Jupiter’s auroral environment. Here we make the assumption that the electron characteristic energies can be used as a proxy. The motivation for this assumption comes from spacecraft studies of in situ particle and field measurements in Earth’s auroral region. In particular, the FAST mission (Carlson et al., 1998) made detailed ion and electron observations as well as D.C. electric field and magnetic field measurements in Earth’s downward and upward current regions. Ergun et al. (1998) compared the D.C. electric field perpendicular to the local magnetic field to both the upgoing ion and electron distributions and found that the total potential derived from each method was in agreement. They note that the electron distributions exhibited a broad energy peak that spanned a decade or more in energy (see their Figure 3)—likely modified due to wave-particle interactions—which added a factor of 2 in error in deriving the total potential drop. The electron distributions observed by Juno/JEDI are more narrowly peaked in energy, and therefore, we expect these errors to be smaller accordingly.

3.4. Comparisons to Juno/JEDI Observations

Figure 4 shows the JEDI data from Figure 2 with the addition of the theoretical curves from equations (4)–(7). The purple and red dashed curves in Figure 4a illustrate the turbulence dissipation theory (equation (7)) for two different electron inertial length scales, 20 and 30 km, respectively. The green and blue curves in Figure 4b represent Knight’s relation with relativistic electron velocities (equation (6)) and with nonrelativistic velocities,

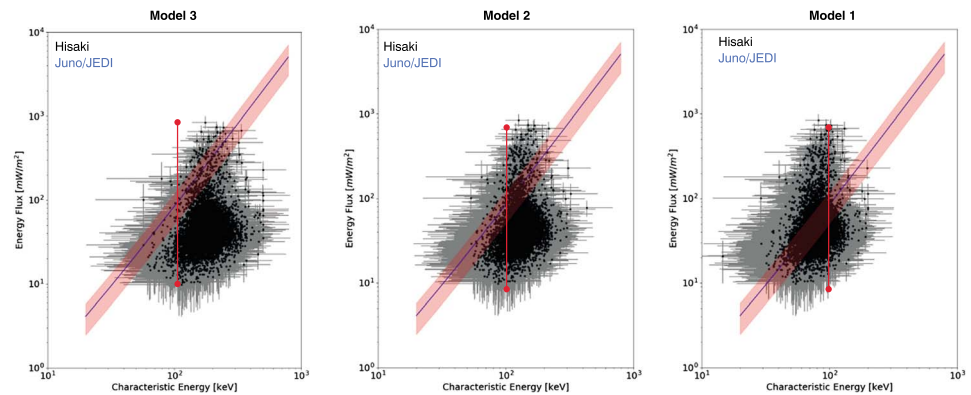


Figure 5. Comparisons between Juno/JEDI and Hisaki remote sensing observations for three different atmospheric models (details in text). The black dots represent Hisaki data with associated errors illustrated by the gray error bars. The blue curve represents the best fit Knight relation curve to the JEDI data with the red envelope depicting the standard deviation ($\sim 30\%$ constant error) of the JEDI measurements. The red vertical bar at ~ 100 keV is an example of the range of energy flux values obtained (factor of 100) by JEDI. JEDI = Jupiter Energetic particle Detector Instrument.

respectively (equations (4) and (5)). In all cases we assume $N = 0.018 \text{ cm}^{-3}$ and $W_{\text{th}} = 2.5 \text{ keV}$ since these parameters were measured by Voyager (Scudder et al., 1981) and used in many other studies (e.g., Cowley & Bunce, 2001; Ray et al., 2010). The multiple blue curves depict the R_B dependence ranging from $R_B \rightarrow \infty$ to $R_B = 27$. At the smaller characteristic energies, the difference between relativistic and nonrelativistic curves are indistinguishable—however, the difference becomes noticeable at the larger energies since the higher-order term due to the relativistic velocities plays a nonnegligible role ($\sim 20\%$ at 300 keV). Similarly, the R_B dependence is greatest at larger characteristic energies. This is because the saturation current or energy flux occurs at smaller energies when the location of the acceleration region is closer to the auroral region. We note that Ray et al. (2010) modeled the various cases of Knight’s relation for smaller R_B between a lower limit of 11 and an upper limit of 27. The upper limit places the acceleration region $\sim 3 R_J$.

We defer the interpretation to section 5, but here we briefly discuss the comparisons. First, it appears the energy flux and characteristic energy derived from JEDI data correlate well with a positive trend and do not roll over as one might expect with the acceleration region placed at the lowest altitudes (see blue curves or equation (4)). Additionally, no single set of temperatures and densities can reconcile the differences between equation (4) and the JEDI observations. The theoretical curves based on turbulence theory and the relativistic Knight relationship with larger values of R_B , do the best job at matching the measurements. It is also remarkable to note how well these two, but very different, theories match over the energy ranges of interest here. Why this happens is not clear. However, the data when separated by the type of acceleration process (broadband vs. discrete) also reveal a very similar trend and both match the theoretical curves well.

4. Comparisons to Remote Sensing Observations From Hisaki

Figure 5 shows the remote sensing observations of Jupiter’s auroral emissions from Hisaki and the comparison to Juno/JEDI. Hisaki data reflect the total emissions integrated over the northern auroral region and covers a 3-year time span from December 2013 to August 2016. For clarity we represent the Juno/JEDI observations by applying equation (5) with $N = 0.018 \text{ cm}^{-3}$ and $W_{\text{th}} = 2.5 \text{ keV}$ (see Figure 4b, blue curve same JEDI parameters for all) and use two methods for illustrating the measurement spread: the standard deviation of the results shown by the semitransparent red envelope; and the full spread in energy flux of electrons with characteristic energies ~ 100 keV (the red vertical line). The three panels in Figure 5 correspond to three different models used to invert the Hisaki measured emissions to infer an electron characteristic energy. Each model uses a different Jovian atmospheric model, methane altitude distribution, and auroral electron distribution. These three models were used in Tao et al.’s (2016) study of the Jovian auroral emissions using Hisaki data. Models 2 and 3 here correspond to models labeled as 1 and 2 in Gérard et al. (2014). As Gérard et al. (2014) points out, our Model 2 is based on the Moses et al. (2005) model *B*, which is based on the

hydrocarbon distribution derived from the ISO satellite measurements, similar to Gladstone et al.'s (1996) profile. The eddy diffusion coefficient used at the methane homopause is $K_H = \sim 3 \times 10^6 \text{ cm}^2/\text{s}$. Here Model 3 is based on the atmospheric density profiles from Grodent et al. (2001) and uses $K_H = 1.4 \times 10^6 \text{ cm}^2/\text{s}$ (Gérard et al., 2014). Lastly, Model 1 uses the model outlined in Gérard et al. (2003), which is based on the neutral atmosphere model from Gladstone et al. (1996) and methane vertical distribution from the lower boundary mixing ratio outlined in Drossart et al. (1993). Here $K_H = 1.4 \times 10^6 \text{ cm}^2/\text{s}$, but the hydrocarbons are transferred upward more efficiently than Models 2 and 3 relative to the other models using the same H_2 column density (Tao et al., 2016). Additionally, Models 2 and 3 assume a monoenergetic electron profile, whereas Model 1 assumes a Maxwellian shape. Gérard et al. (2014) state that "if the distribution is actually Maxwellian but assumed to be monoenergetic, the energy associated with a color ratio of 1.5 would be 50 keV instead of 79 keV in the Maxwellian case."

Both the Hisaki and Juno observations show significant spread in the energy flux for a given characteristic energy. For example, at ~ 100 keV both sets of data show a dynamic range of ~ 100 (~ 10 to 1000 mW/m^2). Regardless of the spread, the comparison between the data sets shows that Model 1 does the best job in matching the Hisaki observations to Juno/JEDI. This is purely a qualitative comparison by noting that Model 1 produces the most significant overlap across the bulk of the observations between approximately 10 and 100 mW/m^2 . The greater than 100 mW/m^2 observations near 100 keV from Hisaki deviate from the apparent linear trend—when the data are shown on a logarithmic scale—but the data are somewhat consistent with the spread in the Juno/JEDI data. Tao et al. (2016) note that the greater than 100 mW/m^2 measurements near 100 keV are observed during times of solar wind dynamic pressure enhancements and are mainly due to variations in the electron number flux rather than the electron energies.

5. Discussion

5.1. MI Coupling Processes

We compare two classes of acceleration theories that have been proposed for Jupiter's main auroral region: turbulence dissipation theory (Figure 4a) and Knight theory (Figure 4b). Surprisingly, both theories predict very similar relationships and the observations appear to support this. In Figure 1b, the Juno/JEDI observations were separated into broadband and discrete/inverted-V distributions and the data show nearly identical energy flux relationships for the two types of distributions. One may question if these two types of distributions are related, for example, can a peaked-energy distribution evolve, through wave-particle interactions, into a broadband energy distribution with no peaks? If that were the case then it would not be surprising that these distributions yield similar relationships. Inspection of electron energy and angle beams by Mauk et al. (2017b) illustrate that both discrete and broadband energy distributions can occur during a single main auroral crossing. They concluded that because the broadband energy distributions have a much larger energy density than the peaked distributions then they could not be the result of simple energy diffusion processes acting on a peaked-energy distribution. This leads us to the conclusion that both discrete and stochastic processes exist in the main auroral region and the relationships for each type appear to have a similar energy flux versus characteristic energy relationship.

The turbulence dissipation model assumes that the electromagnetic field fluctuations are converted into electron energy through wave-particle interaction at scales close to the electron inertial length scale. The expression used here (equation (7)) should only be regarded as a first order estimate. For a full description, detailed quantitative modeling of the associated wave-particle interactions is required.

In Figure 4b, we compared various forms of the Knight relation to the Juno/JEDI observations and found that for cases where the acceleration region was confined to lower altitudes, that is, $R_B = 27$ or $3 R_J$, the curves would roll over and begin to plateau at much smaller energy flux values than measured. The Knight profiles which places the top of the auroral acceleration potential at larger altitudes better represent the data. From this analysis, we suggest that acceleration region may be located at distances larger than $6 R_J$ or $R_B = 216$. Previous studies have considered a range of locations for the acceleration region (e.g., Cowley & Bunce, 2001, Ray et al., 2010). We find that because the data are most consistent with larger values of R_B , the current does not saturate as quickly as predicted by Ray et al. (2010). Additionally, as Ray et al. (2010) mention in their conclusions, the role of the field-aligned potentials and Pedersen conductivities vary with the location of the

acceleration region. Therefore, we believe these comparisons between data and theory will stimulate fruitful discussions for future topics regarding Jovian MI coupling processes.

Nichols and Cowley (2004) examined the effect of the enhanced Pedersen conductivity caused by precipitating electrons in Jupiter's upward current or main auroral region. Their model characterized the precipitating auroral electron distributions as a combination of two power law distributions with the spectral break occurring at the accelerating voltage (see their equation (19) and Figure 3). In Figure 4 of Nichols and Cowley (2004) they show plots of the height integrated Pedersen conductivity versus field-aligned current density for different auroral distributions characterized by their power law function. Using their same notation, α is the spectral slope below the accelerating potential and β is the spectral slope above the potential. They note that for larger currents the conductivity depends more on the spectral slope at the smaller energies (below that produced by the accelerating potential). The auroral distributions observed by JEDI (Figure 3) tend to be flat in intensity below both the peak or rollover depending on the type of distribution being considered. In phase space density, this means the spectral slopes at lower energies are often $\alpha \approx 1$ to 2, or E^{-1} to E^{-2} . The auroral distributions studied by Mauk et al. (2017a, 2018) also show similar spectral shapes at the lower energies. The tail of the distribution at the larger energies, defined as above the peak or rollover in the spectrum, can have spectral slopes that vary dramatically. For example, the broadband distributions tend to be characterized with slopes $\beta \approx 3$ to 6, or E^{-3} to E^{-6} , whereas peaked distributions can have tails that vary as much as $\beta \approx 3$ to 12 or E^{-3} to E^{-12} . Initial analysis using the Nichols and Cowley (2004) model with fixed α and electron number flux indicates that increased β tends to lead to reduced Pedersen conductance at higher current densities, but a full exploration of the effects of such spectral distributions on the Pedersen conductance and the M-I coupling current system is beyond the scope of this paper and will be considered in future works.

Why the auroral electron distributions have their specific shapes is unknown at this time. One hypothesis may be that the harder tails associated with the peaked distributions are due to wave-particle interactions scattering the energy of the electrons, effectively smoothing out the sharp gradients in phase space. The nature of the slope at the lower energies may also be due to wave-particle interactions or energy degradation due to electrons backscattering in the atmosphere; however, future work is needed to explore these ideas.

5.2. Jupiter's Hydrocarbon Distribution in the Auroral Region

We showed in section 4 that the atmospheric model that minimized the discrepancy between the Juno and Hisaki measurements required that hydrocarbons be transported more efficiently to higher altitudes, that is, Model 1. This is not the first observation to suggest such a scenario, but it does offer an independent method that demonstrates the point. Previous work done by Parkinson et al. (2006) used observations from the Cassini Ultraviolet Imaging System (Esposito et al., 2004) during the Jupiter flyby in late 2000 and early 2001. Using intensities from the He 584 Å emission, they were able to constrain radiative transfer models based on increased eddy diffusion mixing in the auroral regions. Their conclusions suggest that K_H may be at least 8×10^6 cm²/s and possibly greater than 4×10^7 cm²/s, which places that 5 to 25 times larger than the nominal value of 1.4×10^6 cm²/s used in the equatorial region.

Gérard et al. (2003) investigated the sensitivity of the inferred electron energies on K_H for a given atmospheric model and found that a factor of 10 increase of K_H only changes the inferred mean or characteristic energies by a factor of ~ 2 (Gérard et al., 2003; see their Figure 2). Conceptually, if Model 2 or Model 3 were chosen (see Figure 5) then to match Juno/JEDI and Hisaki, enhanced eddy diffusion coefficients in the auroral zone must be on the order of 10 times larger or more than the nominal value used in the equatorial region—in agreement with the increase that Parkinson et al. (2006) found. We note that in section 4 the color ratio is also dependent on the electron population assumed in the model, that is, monoenergetic or Maxwellian; however, that has a lesser effect than hydrocarbon column density in Jupiter's atmosphere, so we ignored it for this simple argument.

Enhanced diffusion of the hydrocarbons in the aurora region is only one possible solution, and the basic argument lacks the rigor of a full-scale model that may take into account the shape of the full electron distribution, the detailed interactions between the precipitating electrons and the various types of hydrocarbons, the resultant chemistry due to large-scale electron precipitation, etc. Clearly, caution should be exercised in our interpretations, but it stands to reason that the comparisons between in situ auroral measurements and remote sensing observations are able to help constrain current and future models regarding the

atmospheric content of Jupiter that is otherwise unattainable. In general, the hydrocarbon eddy diffusion coefficient in Jupiter's auroral region is poorly known and our state of knowledge is based on modeling and limited results from the He 584 Å emissions. Future analysis of Juno, Hisaki, and HST data sets and ground-based infrared support (e.g., Sinclair et al., 2017, and references therein) in combination with physical models are needed to further our understanding of this complex region.

6. Summary

In this study, we presented for the first time the greater than 30 keV energy flux versus characteristic energy relationships observed in the loss cone over the main auroral region by Juno/JEDI. The purpose of this study is to provide in situ measurements that can be used to test the current predictions of the various Jovian acceleration theories as well as further constrain the atmospheric models through comparisons with remote sensing observations. We found that by comparing Juno/JEDI data with both Knight (1973; e.g., Cowley, 2006, Cowley & Bunce, 2001, Ray et al., 2009, 2010; Ray & Ergun, 2013) and MHD turbulence (Saur et al., 2003) theories, we could not distinguish a primary driver; however, there is no reason to believe that these mechanisms are mutually exclusive. In fact, the broadband and inverted-V-type auroral electron populations within the loss cone exhibit similar trends and may provide evidence that both processes play an active role in the generation of field-aligned auroral currents that map to the main auroral oval. Additionally, inspection of the electron distribution shapes presented here can help constrain the parameter range, especially for the slopes at the lower energies required to model the effect of electron precipitation on the height integrated Pedersen conductivities (Nichols & Cowley, 2004). It is also interesting to note that we do not observe the energy fluxes to plateau within the energy range JEDI is sensitive to (30 keV to 1 MeV). This may be consistent with the picture that the height at the top of the acceleration region (for Knight theories) is at distances larger than a few Jovian radii.

We found that the atmospheric model that most efficiently transports hydrocarbons to higher altitudes provides the best agreement between the Hisaki and Juno/JEDI data sets. This is *Model 1* labeled in section 4 and Figure 5. Similarly, agreement can also be found if other models, for example, *Model 3* was used and the hydrocarbon eddy diffusion coefficient was increased by a factor of $10 - 30 \times K_H$. Either way, the data suggest that the hydrocarbon densities in the auroral region are likely higher due to precipitating electrons dissipating large amounts of energy (e.g., Parkinson et al., 2006). We should note, however, that this is just one possible solution to a complex problem that involves several free and poorly constrained parameters.>

Acknowledgments

We would like to thank everyone that made the Juno and Hisaki mission a success as well as NASA and JAXA for establishing the Hisaki participating science program, which promotes collaboration and enhances the scientific return of Jupiter observations. G. C. would like to thank Denis Grodent, Vincent Hue, James Sinclair, Mark Perry, Don Mitchell, Brian Anderson, and Jesper Gjerloev for their helpful discussions and support. G. C. would also like to thank Chelsea Clark for copyediting. E. J. B. and J. D. N. are supported by STFC Consolidated grant ST/N000749/1, and E. J. B. is supported by a Royal Society Wolfson Research Merit Award. At time of writing, Juno data for PJs 1–6 are in NASA's planetary data system, and the other data reside in an archive at the John Hopkins University Applied Physics Laboratory (<http://www.jhuapl.edu/jedi>). That site is password controlled, but access for evaluation can be obtained by contacting the lead author of this paper.

References

- Allegrini, F., Bagenal, F., Bolton, S., Connerney, J., Clark, G., Ebert, R. W., et al. (2017). Electron beams and loss cones in the auroral regions of Jupiter. *Geophysical Research Letters*, *44*, 7131–7139. <https://doi.org/10.1002/2017GL073180>
- Carlson, C., McFadden, J. P., Ergun, R. E., Temerin, M., Peria, W., Mozer, F. S., et al. (1998). FAST observations in the downward auroral current region: Energetic upgoing electron beams, parallel potential drops, and ion heating. *Geophysical Research Letters*, *25*(12), 2017–2020. <https://doi.org/10.1029/98GL00851>
- Clark, G., Mauk, B. H., Haggerty, D., Paranicas, C., Kollmann, P., Rymer, A., et al. (2017). Energetic particle signatures of magnetic field-aligned potentials over Jupiter's polar regions. *Geophysical Research Letters*, *44*, 8703–8711. <https://doi.org/10.1002/2017GL074366>
- Clark, G., Mauk, B. H., Paranicas, C., Haggerty, D., Kollmann, P., Rymer, A., et al. (2017). Observation and interpretation of energetic ion conics in Jupiter's polar magnetosphere. *Geophysical Research Letters*, *44*, 4419–4425. <https://doi.org/10.1002/2016GL072325>
- Connerney, J. E. P., Acuña, M. H., & Ness, N. F. (1981). Modeling the Jovian current sheet and inner magnetosphere. *Journal of Geophysical Research*, *86*(A10), 8370–8384. <https://doi.org/10.1029/JA086iA10p08370>
- Connerney, J. E. P., Acuña, M. H., Ness, N. F., & Satoh, T. (1998). New models of Jupiter's magnetic field constrained by the Io flux tube footprint. *Journal of Geophysical Research*, *103*(A6), 11,929–11,939. <https://doi.org/10.1029/97JA03726>
- Connerney, J. E. P., Benn, M., Bjarno, J. B., Denver, T., Espley, J., Jorgensen, J. L., et al. (2017). The Juno magnetic field investigation. *Space Science Reviews*, *213*(1–4), 39–138. <https://doi.org/10.1007/s11214-017-0334-z>
- Cowley, S. W. H. (2006). Current-voltage and kinetic energy flux relations for relativistic field-aligned acceleration of auroral electrons. *Annales de Geophysique*, *24*(1), 325–338. <https://doi.org/10.5194/angeo-24-325-2006>
- Cowley, S. W. H., & Bunce, E. J. (2001). Origin of the main auroral oval in Jupiter's coupled magnetosphere—Ionosphere system. *Planetary and Space Science*, *49*(10–11), 1067–1088. [https://doi.org/10.1016/S0032-0633\(00\)00167-7](https://doi.org/10.1016/S0032-0633(00)00167-7)
- Cowley, S. W. H., Bunce, E. J., Stallard, T. S., & Miller, S. (2003). Jupiter's polar ionospheric flows: Theoretical interpretation. *Geophysical Research Letters*, *30*(5), 1220. <https://doi.org/10.1029/2002GL016030>
- Drossart, P., Bézard, B., Atreya, S. K., Bishop, J., Waite, J. H., & Boice, D. (1993). Thermal profiles in the auroral regions of Jupiter. *Journal of Geophysical Research*, *98*(E10), 18803. <https://doi.org/10.1029/93JE01801>
- Ebert, R. W., Allegrini, F., Bagenal, F., Bolton, S. J., Connerney, J. E. P., Clark, G., et al. (2017). Spatial distribution and properties of 0.1–100 keV electrons in Jupiter's polar auroral region. *Geophysical Research Letters*, *44*, 9199–9207. <https://doi.org/10.1002/2017GL075106>
- Elliott, S. S., Gurnett, D. A., Kurth, W. S., Clark, G., Mauk, B. H., Bolton, S. J., et al. (2018). Pitch angle scattering of upgoing electron beams in Jupiter's polar regions by whistler mode waves. *Geophysical Research Letters*, *45*, 1246–1252. <https://doi.org/10.1002/2017GL076878>

- Ergun, R. E., Carlson, C. W., McFadden, J. P., Mozer, F. S., Delory, G. T., Peria, W., et al. (1998). FAST satellite observations of electric field structures in the auroral zone. *Geophysical Research Letters*, 25(12), 2025–2028. <https://doi.org/10.1029/98GL00635>
- Esposito, L. W., et al. (2004). The Cassini ultraviolet imaging spectrograph investigation. *Space Science Reviews*, 115, 299–361.
- G erard, J., Bonfond, B., Grodent, D., Radioti, A., Clarke, J. T., Gladstone, G. R., et al. (2014). Mapping the electron energy in Jupiter's aurora: Hubble spectral observations. *Journal of Geophysical Research*, 9072–9088. <https://doi.org/10.1002/2014JA020514>
- G erard, J. C., Gustin, J., Grodent, D., Clarke, J. T., & Grard, A. (2003). Spectral observations of transient features in the FUV Jovian polar aurora. *Journal of Geophysical Research: Space Physics*, 108(A8), 1319. <https://doi.org/10.1029/2003JA009901>
- Gladstone, G. R., Allen, M., & Yung, Y. L. (1996). Hydrocarbon photochemistry in the upper atmosphere of Jupiter. *Icarus*, 119(1), 1–52. <https://doi.org/10.1006/icar.1996.0001>
- Grodent, D. (2015). A brief review of ultraviolet Auroral emissions on Giant planets. *Space Science Reviews*, 187(1–4), 23–50. <https://doi.org/10.1007/s11214-014-0052-8>
- Grodent, D., Waite, J. H., & Gerard, J. C. (2001). A self-consistent model of the Jovian auroral structure. *Journal of Geophysical Research*, 106(A7), 12,933–12,952. <https://doi.org/10.1029/2000JA900129>
- Gustin, J., G erard, J. C., Grodent, D., Cowley, S. W. H., Clarke, J. T., & Grard, A. (2004). Energy-flux relationship in the FUV Jovian aurora deduced from HST-STIS spectral observations. *Journal of Geophysical Research*, 109, A10205. <https://doi.org/10.1029/2003JA010365>
- Haggerty, D. K., Mauk, B. H., Paranicas, C. P., Clark, G., Kollmann, P., Rymer, A. M., et al. (2017). Juno/JEDI observations of 0.01 to >10 MeV energetic ions in the Jovian auroral regions: Anticipating a source for polar X-ray emission. *Geophysical Research Letters*, 44, 6476–6482. <https://doi.org/10.1002/2017GL072866>
- Hess, S. L. G., Bonfond, B., Zarka, P., & Grodent, D. (2011). Model of the Jovian magnetic field topology constrained by the Io auroral emissions. *Journal of Geophysical Research*, 116, A05217. <https://doi.org/10.1029/2010JA016262>
- Hill, T. W. (1979). Inertial limit on corotation. *Journal of Geophysical Research*, 84(A11), 6554. <https://doi.org/10.1029/JA084iA11p06554>
- Hill, T. W. (2001). The Jovian auroral oval. *Journal of Geophysical Research*, 106(A5), 8101–8107. <https://doi.org/10.1029/2000JA000302>
- Hill, T. W., Dessler, A. J., & Maher, L. J. (1981). Corotating magnetospheric convection. *Journal of Geophysical Research*, 86(A11), 9020–9028. <https://doi.org/10.1029/JA086iA11p09020>
- Khurana, K. K. (2001). Influence of solar wind on Jupiter's magnetosphere deduced from currents in the equatorial plane. *Journal of Geophysical Research*, 106, 25,999–26,016. <https://doi.org/10.1029/2000JA000352>
- Kivelson, M. G., Bagenal, F., Neubauer, F. M., Kurth, W., Paranicas, C., & Saur, J. (2004). Magnetospheric interactions with satellites. In F. Bagenal (Ed.), *Jupiter* (Chap. 21, pp. 513–536). New York: Cambridge University Press.
- Knight, S. (1973). Parallel electric fields. *Planetary and Space Science*, 21(5), 741–750. [https://doi.org/10.1016/0032-0633\(73\)90093-7](https://doi.org/10.1016/0032-0633(73)90093-7)
- Li, W., Thorne, R. M., Ma, Q., Zhang, X. J., Gladstone, G. R., Hue, V., et al. (2017). Understanding the origin of Jupiter's diffuse aurora using Juno's first perijove observations. *Geophysical Research Letters*, 44, 10,162–10,170. <https://doi.org/10.1002/2017GL075545>
- Louarn, P., Allegrini, F., McComas, D. J., Valek, P. W., Kurth, W. S., Andr e, N., et al. (2017). Generation of the Jovian hectometric radiation: First lessons from Juno. *Geophysical Research Letters*, 44, 4439–4446. <https://doi.org/10.1002/2017GL072923>
- Ma, Q., Thorne, R. M., Li, W., Zhang, X. J., Mauk, B. H., Paranicas, C., et al. (2017). Electron butterfly distributions at particular magnetic latitudes observed during Juno's perijove pass. *Geophysical Research Letters*, 44, 4489–4496. <https://doi.org/10.1002/2017GL072983>
- Mauk, B. H., Haggerty, D. K., Jaskulek, S. E., Schlemm, C. E., Brown, L. E., Cooper, S. A., et al. (2017). The Jupiter Energetic Particle Detector Instrument (JEDI) investigation for the Juno mission. *Space Science Reviews*, 213(1–4), 289–346. <https://doi.org/10.1007/s11214-013-0025-3>
- Mauk, B. H., Haggerty, D. K., Paranicas, C., Clark, G., Kollmann, P., Rymer, A. M., et al. (2017b). Discrete and broadband electron acceleration in Jupiter's powerful aurora. *Nature*, 549(7670), 66–69. <https://doi.org/10.1038/nature23648>
- Mauk, B. H., Haggerty, D. K., Paranicas, C., Clark, G., Kollmann, P., Rymer, A. M., et al. (2017a). Juno observations of energetic charged particles over Jupiter's polar regions: Analysis of monodirectional and bidirectional electron beams. *Geophysical Research Letters*, 44, 4410–4418. <https://doi.org/10.1002/2016GL072286>
- Mauk, B. H., Haggerty, D. K., Paranicas, C. P., Clark, G., Kollmann, P., Rymer, A. M., et al. (2018). Diverse electron and ion acceleration characteristics observed over Jupiter's main aurora. *Geophysical Research Letters*, 1277–1285. <https://doi.org/10.1002/2017GL076901>
- Mauk, B. H., Mitchell, D. G., McEntire, R. W., Paranicas, C. P., Roelof, E. C., Williams, D. J., et al. (2004). Energetic ion characteristics and neutral gas interactions in Jupiter's magnetosphere. *Journal of Geophysical Research*, 109, A09S12. <https://doi.org/10.1029/2003JA010270>
- McComas, D. J., Alexander, N., Allegrini, F., Bagenal, F., Beebe, C., Clark, G., et al. (2017). The Jovian Auroral Distributions Experiment (JADE) on the Juno mission to Jupiter. *Space Science Reviews*, 213(1–4), 547–643. <https://doi.org/10.1007/s11214-013-9990-9>
- Moses, J. I., Fouchet, T., B ezard, B., Gladstone, G. R., Lellouch, E., & Feuchtgruber, H. (2005). Photochemistry and diffusion in Jupiter's stratosphere: Constraints from ISO observations and comparisons with other giant planets. *Journal of Geophysical Research*, 110, E08001. <https://doi.org/10.1029/2005JE002411>
- Nichols, J., & Cowley, S. (2005). Magnetosphere-ionosphere coupling currents in Jupiter's middle magnetosphere: Effect of magnetosphere-ionosphere decoupling by field-aligned auroral voltages. *Annales Geophysicae*, 2004, 799–808. Retrieved from <http://hal.archives-ouvertes.fr/hal-00317613/>
- Nichols, J. D., & Cowley, S. W. H. (2004). Magnetosphere-ionosphere coupling currents in Jupiter's middle magnetosphere: Effect of precipitation-induced enhancement of the ionospheric Pedersen conductivity. *Annales Geophysicae*, 22(5), 1799–1827. <https://doi.org/10.5194/angeo-22-1799-2004>
- Parkinson, C. D., Stewart, A. I. F., Wong, A. S., Yung, Y. L., & Ajello, J. M. (2006). Enhanced transport in the polar mesosphere of Jupiter: Evidence from Cassini UVIS helium 584   airglow. *Journal of Geophysical Research*, 111, E02002. <https://doi.org/10.1029/2005JE002539>
- Ray, L. C., & Ergun, R. E. (2013). Auroral signatures of ionosphere-magnetosphere coupling at Jupiter and Saturn. *Auroral Phenomenology and Magnetospheric Processes: Earth and Other Planets*, 205–214. <https://doi.org/10.1029/2011GM001172>
- Ray, L. C., Ergun, R. E., Delamere, P. A., & Bagenal, F. (2010). Magnetosphere-ionosphere coupling at Jupiter: Effect of field-aligned potentials on angular momentum transport. *Journal of Geophysical Research*, 115, A09211. <https://doi.org/10.1029/2010JA015423>
- Ray, L. C., Su, Y. J., Ergun, R. E., Delamere, P. A., & Bagenal, F. (2009). Current-voltage relation of a centrifugally confined plasma. *Journal of Geophysical Research*, 114, A04214. <https://doi.org/10.1029/2008JA013969>
- Saur, J., Politano, H., Pouquet, A., & Matthaeus, W. (2002). Evidence for weak MHD turbulence in the middle magnetosphere of Jupiter. *Astronomy & Astrophysics*, 386(2), 699–708. <https://doi.org/10.1051/0004-6361:20020305>
- Saur, J., Pouquet, A., & Matthaeus, W. H. (2003). An acceleration mechanism for the generation of the main auroral oval on Jupiter. *Geophysical Research Letters*, 30(5), 1260. <https://doi.org/10.1029/2002GL015761>
- Scudder, J. D., Sittler, E. C., & Bridge, H. S. (1981). A survey of the plasma electron environment of Jupiter: A view from Voyager. *Journal of Geophysical Research*, 86(A10), 8157–8179. <https://doi.org/10.1029/JA086iA10p08157>

- Sinclair, J. A., Orton, G. S., Greathouse, T. K., Fletcher, L. N., Tao, C., Gladstone, G. R., et al. (2017). Independent evolution of stratospheric temperatures in Jupiter's northern and southern auroral regions from 2014 to 2016. *Geophysical Research Letters*, *44*, 5345–5354. <https://doi.org/10.1002/2017GL073529>
- Tao, C., Kimura, T., Badman, S. V., André, N., Tsuchiya, F., Murakami, G., et al. (2016). Variation of Jupiter's aurora observed by Hisaki/EXCEED: 2. Estimations of auroral parameters and magnetospheric dynamics. *Journal of Geophysical Research, A: Space Physics*, *121*, 4055–4071. <https://doi.org/10.1002/2015JA021272>
- Yoshikawa, I., Yoshioka, K., Murakami, G., Yamazaki, A., Tsuchiya, F., Kagitani, M., et al. (2014). Extreme ultraviolet radiation measurement for planetary atmospheres/magnetospheres from the Earth-orbiting spacecraft (Extreme Ultraviolet Spectroscopy for Exospheric Dynamics: EXCEED). *Space Science Reviews*, *184*(1–4), 237–258. <https://doi.org/10.1007/s11214-014-0077-z>